

# Cargo Size Limits and Forces of Cell-Driven Microtransport

Setareh Sharifi Panah, Robert Großmann, Valentino Lepro, and Carsten Beta\*

The integration of motile cells into biohybrid microrobots offers unique properties such as sensitive responses to external stimuli, resilience, and intrinsic energy supply. Here, biohybrid cell–cargo systems that are driven by amoeboid *Dictyostelium discoideum* cells are studied and how the cargo speed and the resulting viscous drag force scales with increasing radius of the spherical cargo particle are explored. Using a simplified geometrical model of the cell–cargo interaction, the findings toward larger cargo sizes, which are not accessible with the experimental setup, are extrapolated and a maximal cargo size is predicted beyond which active cell-driven movements will stall. The active forces exerted by the cells to move a cargo show mechanoresponsive adaptation and increase dramatically when challenged by an external pulling force, a mechanism that may become relevant when navigating cargo through complex heterogeneous environments.

## 1. Introduction

Soft-bodied micromachines with bio-inspired modes of locomotion, such as crawling or swimming, are essential to fulfill many demanding mechanical tasks on the micron scale, including targeted drug delivery. Examples include both synthetic<sup>[1,2]</sup> as well as biohybrid microcarriers, mostly based on cellular microswimmers.<sup>[3–9]</sup> The ability to maneuver through confined, structured terrains,<sup>[5,10,11]</sup> the multi modal locomotion on surfaces with varying adhesion properties,<sup>[12,13]</sup> and the targeted delivery of cargo particles<sup>[14,15]</sup> are examples of recent advancements in developing soft, crawling micromachines. Yet, many challenges remain, including questions of power supply, sensing capacities, and long-term retention that are common to many small-scale robots.<sup>[2,12,16–19]</sup> Ideally, the unique energy efficiency, along with the integrated sensing machinery of biological cells, can be directly harnessed in a biohybrid approach, where motile

cells are combined with synthetic components to a functional device.<sup>[4,5,18–21]</sup>

In this spirit, motivated by the motile capacities of amoeboid cells and by their widespread occurrence,<sup>[22]</sup> we recently proposed a biohybrid microcarrier that operates by directly loading a piece of micro-cargo onto a motile amoeboid cell.<sup>[14,15]</sup> As the active driving element, we used cells of the social amoeba *Dictyostelium discoideum* (*D. discoideum*) that carried different micronsized cargo particles. Owing to the highly nonspecific adhesive properties of these cells,<sup>[23,24]</sup> the physical link between the cargo and the carrier is established spontaneously upon collision, without additional surface functionalizations. The cargo is then subjected to the forces exerted by the motile cell

leading to displacements of the cargo. As the crawling locomotion of *D. discoideum* shares many similarities with the motility of leukocytes that travel through narrow, confined environments during an inflammatory response,<sup>[22,25–29]</sup> it makes them a valuable model organism to study the transport capacities of motile eukaryotic cells. Moreover, *D. discoideum* cells exhibit well-known chemotactic properties<sup>[30]</sup> that can be leveraged to achieve directed microtransport. To demonstrate the capacity of our system for directed transport, we exposed *D. discoideum* cells that were loaded with spherical microparticles of radius 14.5  $\mu\text{m}$  to a chemo-attractant point source. The chemotactic cells followed both static (Movie S1, Supporting Information) and dynamic (Movie S2, Supporting Information) gradient signals, thereby transporting the cargo particles in a directional manner.

In this work, we explore the potentials and limitations of this biohybrid transport system, which we will also refer to hereafter as “cell–cargo system”. We first investigate the active forces exerted by the cell on the cargo as well as the limiting cargo size for microparticle transport in an open, isotropic fluid environment. Using high-speed live cell imaging, we show that only minimal forces up to average values of  $\approx 1$  pN are exerted on spherical cargo particles. Based on a simplified geometrical model for the cell–cargo interaction, we estimate that beyond a limiting cargo radius of  $\approx 123$   $\mu\text{m}$ , cells will, on average, no longer displace the particle. Note that these peak forces arise from the random micromotion of the cargo around the cell and do not depend on the presence of an additional slow, gradient-induced bias of the overall motion. For this reason, we decided to base our analysis on data from cell–cargo systems in the absence of external gradients, which is much easier to acquire reproducibly and in sufficient amounts. Finally, we also use a microfluidic chamber to expose the cell–cargo system to a Poiseuille flow that allows us to probe

S. Sharifi Panah, R. Großmann, V. Lepro, C. Beta  
Institute of Physics and Astronomy  
University of Potsdam  
Karl-Liebknecht Straße 24/25, 14476 Potsdam, Germany  
E-mail: beta@uni-potsdam.de

 The ORCID identification number(s) for the author(s) of this article can be found under <https://doi.org/10.1002/smll.202304666>

© 2023 The Authors. Small published by Wiley-VCH GmbH. This is an open access article under the terms of the Creative Commons Attribution-NonCommercial-NoDerivs License, which permits use and distribution in any medium, provided the original work is properly cited, the use is non-commercial and no modifications or adaptations are made.

DOI: 10.1002/smll.202304666

the response of the cell–cargo system to an external force pulling on the cargo particle. Here, we measure significantly larger forces of up to 0.5 nN, suggesting that the forces generated by the cell may adapt and significantly increase when challenged by an external impact.

## 2. Results

### 2.1. Large-Scale Transport is Suppressed with Increasing Cargo Size

In **Figure 1a**, a microscopy image of a single amoeboid cell carrying a spherical microcargo is displayed, along with the tracks of the cell and the cargo particle shown in red and blue, respectively (see Movie S3, Supporting Information). A corresponding cartoon of this biohybrid cell–cargo system and the spatial coordinates of the system are illustrated in **Figure 1b**. We have previously shown in ref. [15] that the dynamics of this cell–cargo system exhibits two regimes, 1) an idling rest state, where the cargo particle dwells at a constant equilibrium distance  $l_0$  from the cell center and performs circling movements around the cell, and 2) intermittent transition phases during which the cell passes underneath the cargo and continues moving persistently for a while (cf. **Figure 1c** for a cell trajectory shown in the frame of reference of the cargo, where episodes of circling motion and intermittent transitions can be clearly distinguished). The transitions are initiated by bursts in cell polarity toward the cargo particle, most likely triggered by the mechanical impact of the cargo; their duration seems related to the intrinsic lifetime of cell polarity.<sup>[15]</sup> This pattern is also reflected in the temporal dynamics of the distance  $l(t)$  between the cell and cargo centers of mass, displayed in **Figure 1d** for a cargo particle with a radius of 23  $\mu\text{m}$ , where spikes of values in  $l$  reaching below the equilibrium distance (dashed red line) represent transition events. The two dynamical regimes are also reflected in the histogram of  $l$ -values taken over the experimentally recorded time series. The main contribution to the histogram is due to fluctuations around  $l_0$  during the rest state, while the transitions contribute a second smaller peak at lower values of  $l$ , resulting in an asymmetric histogram shape (see **Figure 1e**).

A similar pattern was observed for all recorded particle radii ranging from 5 to 62  $\mu\text{m}$ . Whereas the equilibrium distance  $l_0$  of the rest state increases with increasing particle size, the polarization rate  $\lambda$ , at which transitions occur, decreases.<sup>[15]</sup> Previously, we have proposed an active particle model to account for the specific features of this intermittent colloid dynamics driven by a cell.<sup>[15]</sup> In particular, this modeling approach enabled us to calculate the long-time diffusion coefficient  $D$  of the colloid as a function of the polarization rate  $\lambda$ ; in the absence of polarity bursts ( $\lambda = 0$ ), active transport vanishes and the diffusivity of the cell–cargo system decays to the value of the idling rest state. For the present study, we extended our previous dataset to particles with a radius of 62  $\mu\text{m}$  and extrapolated the decreasing polarization rate as a function of increasing particle radius to estimate the limiting particle size for which the polarization rate decays to zero, see **Figure 1f**. From this estimate, we conclude that no transitions occur—thus, phases of persistent, polar movement will be absent—for particles with a radius that is larger than 85  $\mu\text{m}$  (examples of cell–cargo systems with the corresponding cargo sizes

can be seen in Movies S3–S8, Supporting Information). In the absence of transitions, the active large-scale transport vanishes, reducing the dynamics of the system to circling of the cargo around the cell. Therefore, the long-time diffusivity of the cell–cargo system should be determined by the diffusion coefficient of the carrier cell alone.

### 2.2. Cargo Speed Does not Decrease with Increasing Cargo Radius for Intermediate Cargo Sizes

In what follows, we will concentrate on the forces that the cell exerts on the cargo while moving it. The force estimates do not depend on a non-zero polarization rate, as the cell exerts active forces onto the cargo also during the rest state, resulting in the characteristic circling motion around the cell. We estimated the active force from the cargo speed by taking it to be approximately equal to the drag force that the cargo would experience when being displaced by the cell in a surrounding viscous medium: the drag force on a sphere moving in an open viscous fluid at low Reynolds number is given by Stokes' law,  $F = 6\pi\eta Rv$ , where  $R$  is the radius of the sphere,  $\eta$  the viscosity of medium (here, taken to be equal to the viscosity of water at 20 °C), and  $v$  is the speed of the sphere. The force estimate thus depends on the instantaneous speed of the cargo.

In our experimental setup, the carrier cell interacts with a particle close to the substrate surface. To account for the effect of the planar wall on the drag force, we rely on the solution presented in ref. [31]. It results in a correction factor to the Stokes force that depends on the ratio of the particle radius to its distance  $\delta$  from the wall, see **Figure S1a**, Supporting Information for the dependency of the correction factor on the particle's distance from the wall. As the exact distance between the particle and the wall is not accessible from our experimental recordings and will also change over time due to movement and deformations of the cell, we assume an average distance of  $\delta = 5 \mu\text{m}$  between the particle and the wall, that is, a distance of the same order of magnitude as the cell height.<sup>[32,33]</sup> In this scenario, we obtain a correction factor within the range of 1.4–2.8 for the particle sizes used in our experiments, see **Figure S1b**, Supporting Information.

To resolve peaks in cargo speed and thereby also in active force that occurred during the microtransport, we performed recordings of the microtransport process with a temporal resolution of up to  $\Delta t = 0.2 \text{ s}$ , which is much shorter than the typical timescale of cargo motion. The positions of the cell and the cargo were defined as the centers of mass of the connected identified regions, determined in every time frame through image segmentation (see Experimental Section for details). The instantaneous speeds of the cells and cargo particles were then calculated by finite differences. Note that imaging noise and finite pixel resolution led to small fluctuations in boundary detection and center of mass calculation between consecutive frames. This resulted in small errors in the displacements, which were amplified to large speed fluctuations by the small time step. In order to avoid this artifact, trajectories were smoothed by moving averages prior to calculating the speed values. The smoothing window was determined for every track individually from the correlation time of the original velocities as explained in Experimental Section. **Figure 2a** shows

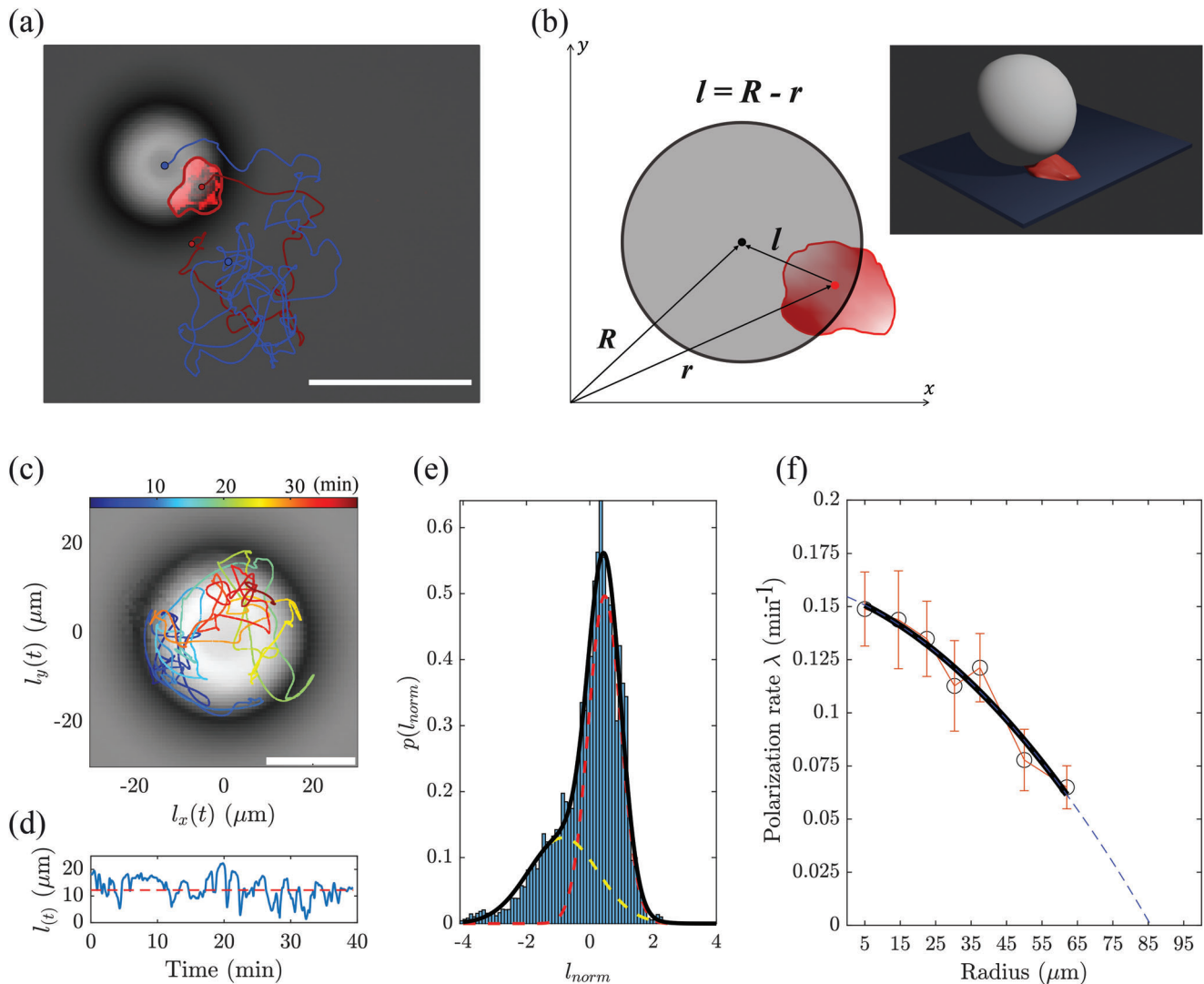


**Figure 1.** Illustration and characteristic dynamics of the cell–cargo system. a) An example of a microscopy image of the cell–cargo system along with trajectories of the cell and the cargo depicted in red and blue, respectively (Movie S3, Supporting Information). The red fluorescence signal marks the F-actin density of the cell. The segmented cell contour is shown with a solid red line. The light gray sphere, encircled with a darker ring in the bright-field image, is the cargo particle with a radius of 23  $\mu\text{m}$ . b) Main geometrical quantities of the system. The vectors  $r$  and  $R$  denote the cell and the cargo positions, respectively. The vector  $l = R - r$  quantifies the relative cargo position with respect to the cell. A 3D rendering of the cell–cargo system is provided as an inset. c) Dynamics of the cell in the frame of reference of the cargo, with the microscopy image of the cargo particle in the background. The transitions can be distinguished from episodes of circling motion. The time is color-coded from blue (beginning) to red (end). d) Temporal changes in the distance  $l(t) = |l(t)|$  between the cell and the cargo centers of mass, shown for a particle with a radius of 23  $\mu\text{m}$ . The red dashed line marks the equilibrium distance  $l_0$ . The polarization rates shown in (f) are derived from the frequency of the peaks extending below  $l_0$ . e) Histogram of the normalized cell–cargo distances  $l_{\text{norm}} = (l - \langle l \rangle) / \text{std}(l)$  for a cell–cargo system with a cargo of radius 23  $\mu\text{m}$ . In order to correct for cell-to-cell variability, the average cell–cargo distance  $\langle l \rangle$  was subtracted from the recorded time series  $l(t)$  and, subsequently, divided by the standard deviation for each trajectory. A double Gaussian distribution is fitted to the asymmetric shape of the histogram (black solid line), capturing the two states of the system dynamics. The major fraction of  $l$  values belongs to the idling rest state with values fluctuating around  $l_0$  (peak of the dashed red Gaussian); a second fraction, covering smaller  $l$  values, represents the transition states (dashed yellow Gaussian). f) Monotonous decay of the polarization rate  $\lambda$  as a function of particle radius along with a parabolic fit (solid black line). The blue dashed line is the extension of the parabolic fit up to a particle radius of  $\approx 85 \mu\text{m}$ , where the transition rate decays to zero. See Experimental Section for details of how the polarization rates are calculated.

an example of the original cell (blue) and cargo tracks (red), in comparison to the smoothed trajectories (overlaid in black).

In Figure 2b, the speed distributions for cargo particles with radii ranging from 14.5 to 62  $\mu\text{m}$  are shown. They exhibit an asymmetric shape with a pronounced peak at speed values  $\approx 10 \mu\text{m min}^{-1}$  and a tail ranging up to speeds of  $\approx 100 \mu\text{m min}^{-1}$ .

Except for the speed distribution of the 14.5  $\mu\text{m}$  particles that displays a more pronounced peak and a more rapid decay, all other distributions closely overlap. This is also reflected in the mean speed values that are similar for all cargo sizes, except for the 14.5  $\mu\text{m}$  particles that move at significantly smaller average speeds, see Figure 2c. For particles with a radius of 23  $\mu\text{m}$

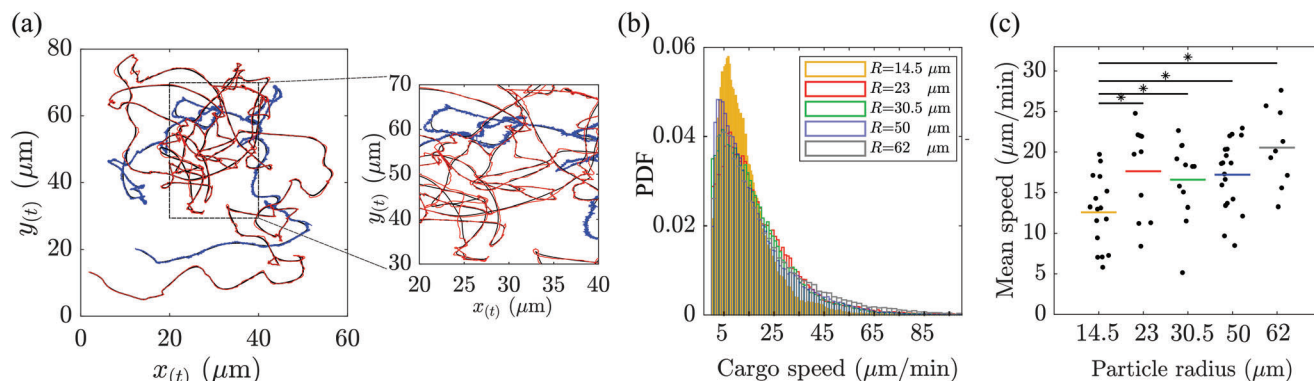


**Figure 2.** Statistics of instantaneous cargo speeds. a) Comparison between the original tracked positions of the cell (red) and the cargo (blue), with the smoothed trajectories (overlaid black lines). The smoothing windows (moving average) are 150 frames (30 s) for the cell and 43 frames (8 s) for the cargo, respectively. b) Cargo speed distribution for each group of measured particle sizes. Only the particle group with  $R = 14.5 \mu\text{m}$  (yellow distribution) shows a pronounced peak at lower speed values; others are practically indistinguishable. c) Mean cargo speed for each trajectory depicted as black data points that belong to the particle radii of  $R = 14.5 \mu\text{m}$  ( $n = 16$ ),  $R = 23 \mu\text{m}$  ( $n = 10$ ),  $R = 30.5 \mu\text{m}$  ( $n = 12$ ),  $R = 50 \mu\text{m}$  ( $n = 19$ ) and  $R = 62 \mu\text{m}$  ( $n = 9$ ). The color-coded lines represent the averaged mean speeds for each group of particles (color-code is identical to the panel b). A two-sample Kolmogorov–Smirnov test reveals that the speed statistics of cargo particles with a radius of  $R = 14.5 \mu\text{m}$  is significantly different from larger particles (significance level:  $\alpha = 0.05$ ), indicated by a star (\*); others are practically identical, that is, the speed statistics of cargoes does not significantly depend on the cargo radius for  $R \geq 23 \mu\text{m}$ .

and larger, a mean cargo speed equal to  $18 \pm 2.4 \mu\text{m min}^{-1}$  (mean $\pm$ std) was observed, notably fairly independent of the particle radius  $R$ .

### 2.3. Only Femto-Newton Forces are Required to Move the Cargo Particles

From the cargo speeds, we calculated the active forces that are necessary to displace the cargo particles based on Stokes' law. As we found similar speeds for cargo radii between 23 and 62  $\mu\text{m}$ , the force according to Stokes' law increased with particle size. We found mean forces ranging from 101 fN for 14.5  $\mu\text{m}$  particles to 949 fN for 62  $\mu\text{m}$  particles, see Figure 3a. To estimate the maximum force applied to the cargo, we considered those episodes of

transport with the highest (95th percentile) speeds. On average, the maximum force also increased with particle size and reached values of up to 2.6 pN applied to particles with a radius of 62  $\mu\text{m}$ , see Figure 3b.

How will the cargo speeds and the active force applied by the carrier cell evolve for larger cargo particles? Unfortunately, the acquisition of reliable data in statistically sufficient amounts became more and more difficult with increasing cargo size; for particles with a radius of more than 62  $\mu\text{m}$ , it turned out to be practically impossible: due to the large dimensions of the cargo in these cases, longer time series, where a single cell interacts with one cargo particle only, are difficult to capture. Furthermore, it has often remained unclear in these situations, whether a neighboring cell is in physical contact with the cargo particle or not

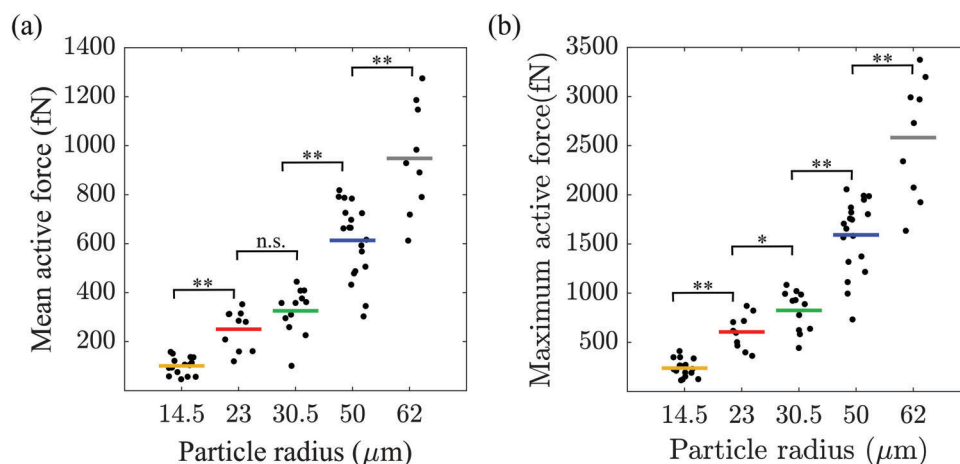


**Figure 3.** Active forces exerted on the cargo. a) On average, the active force  $F$  increases as a function of particle radius. Black data points represent the mean active force measured for each trajectory. The color-coded lines indicate the averaged mean force  $F$  for each group of particles. b) Black data points represent the maximum force (95th percentile) recorded for every single trajectory. The color-coded lines represent the averaged maximum forces for each group of particles. Brackets with one (\*) or two stars (\*\*) indicate a statistically significant increase of the force (Kolmogorov–Smirnov test with significance levels  $\alpha = 0.05$  and  $\alpha = 10^{-3}$ , respectively; n.s. stands for not significant).

when very small colloid displacements were recorded. In order to find out how the active force behaves for larger cargo sizes, we thus have to rely on modeling assumptions to extrapolate from the regime of our experimental observations to the speeds and corresponding forces that are expected for larger particles.

#### 2.4. Geometrical Model for the Speed of the Cell–Cargo Contact Point

Our experimental results showed that cells displace cargoes of very different sizes, ranging from a radius of 14.5 to 62  $\mu\text{m}$ , with similar speeds. According to Stokes' law, a cell thus exerts higher forces on larger cargo sizes, a counter-intuitive observation that we will discuss in more detail in Section 3. Here, we propose a simplified geometrical model that we refer to as the “lever arm model” to interpret our findings in terms of the cell–cargo contact point, which will allow us to predict the cargo speed and active force beyond the experimentally accessible regime of cargo sizes. In particular, we will estimate the maximum active force a cell exerts on a spherical cargo particle and the stalling point of active transport.

The concept of the lever arm model is based on the simplifying idea of reducing the complex and extended cell–cargo contact area to a single contact point. **Figure 4a** shows the overall geometry of the microtransport system in a side view; the corresponding top view can be seen in the inset. We define the cell–cargo contact point as the location, where the line that connects the center of mass of the cell–substrate contact area with the center of the spherical cargo particle, intersects the cargo surface, marked as  $O$  in **Figure 4a**. Its projection  $C$  into the cell–substrate plane lies on the line that connects the centers of mass of cell and cargo in our 2D microscopy images [vector  $l(t)$ ], confer **Figure 4a**. Assuming that the cargo particle moves at an average height of  $\approx 5 \mu\text{m}$  above the substrate, we can calculate the position  $r_c(t)$  of the projected cell–cargo contact point  $C$  as seen from the center of mass of the cell, using the positions  $r(t)$  and  $R(t)$  of the cell and cargo, respectively, in our 2D microscopy images. The position of the projected cell–cargo contact point is then given by

$$r_c(t) = \frac{l_c(t)}{l(t)} \cdot [R(t) - r(t)] \quad (1)$$

with

$$l_c(t) = l(t) - \frac{Rl(t)}{\sqrt{(R + \delta)^2 + l^2(t)}} \quad (2)$$

denoting the distance from the center of mass of the cell–substrate contact area to the projected cell–cargo contact point  $C$ , depending on the cell–cargo distance  $l(t)$  and the radius  $R$  of the cargo particle;  $\delta$  is taken to be equal to 5  $\mu\text{m}$ . As movements of the cell–cargo contact point  $O$  in vertical direction will be much smaller than the lateral movements, reflected by the circling motion of the cargo around the cell, we will estimate the speed of the cell–cargo contact point from the speed of its projection  $C$  in the cell–substrate plane.

Note that Equation (1) critically depends on the condition that the cargo is moving in close proximity to the substrate. For larger

cargo sizes, transitions become rare, see **Figure 1f**. In this regime, the cargo dynamics is limited to circular motion around the cell, so that we can safely assume that the cargo remains close to the substrate. For smaller cargoes, however, this is not necessarily the case. To estimate the contact point speed, we therefore rely only on the cargo speed values taken from those episodes of the data for which the condition  $l(t) \geq l_0$  is fulfilled, that is, for which the cell–cargo distance  $l(t)$  is equal or larger than the equilibrium distance  $l_0$  (during the rest state), so that we can assume that the cargo is close to the substrate, thereby excluding transitions from the data analysis. The data analysis revealed that force maxima appear not only during the transitions but also during the resting state, when the cargo particle circles around the cell at a fixed distance (see **Figure 4c,d**, where the trajectory of the cargo, seen from the frame of reference of the cell, is shown with a color-code corresponding to the cargo speed). We are thus confident that maxima of the active force can be also reliably estimated from cargo trajectories excluding the transition events.

#### 2.5. Speed of the Cell–Cargo Contact Point Decreases with Cargo Size Predicting an Upper Size Limit for Active Transport

Based on the geometrical model introduced above, we now ask how the speed of the cell–cargo contact point will evolve for larger cargoes and what limiting cargo size the cell will fail to move. Finding these limits will also provide an estimate of the maximum force that a single agent cell applies to the cargo during transport in an isotropic viscous fluid environment.

After excluding the transition periods as described above, we determined the position  $r_c(t)$  of the cell–cargo contact point as seen from the center of mass of the cell according to Equation (1). In the laboratory frame of reference, the position of the cell–cargo contact point is thus given by  $R_c(t) = r(t) + r_c(t)$  and its speed by the time derivative of  $R_c(t)$ . Since the speed of the cell is much smaller than the speed of the cargo particle (by about a factor of 5 on average, see **Figure S3**, Supporting Information), we approximate the speed of the contact point by  $\dot{R}_c(t) \approx \dot{r}_c(t)$ , thus assuming that the cell remains stationary at the timescale of interest and the cargo circles around it. The resulting contact point speeds for different cargo sizes can be seen in **Figure 5a**. While the speed of the cargo remained roughly constant for intermediate particle sizes, the contact point speed decreases (see Supporting Information for details of the contact point speed statistics, in particular **Figure S4**, Supporting Information). This can be understood as a consequence of the geometry of the system that is represented in a simplified fashion by our lever arm model, see **Figure 4b**. Spheres that are displaced at similar speeds along circular trajectories around the cell will exhibit a decreasing cell–cargo contact point speed for increasing radius  $R$  of the spherical cargo particles.

We applied linear regression to the contact point speed as a function of the particle radius and extrapolated the fit function to find a critical cargo radius of 123  $\mu\text{m}$ , where the contact point speed decreased to zero. From the uncertainty of the fitting parameters, we expect the critical cargo radius to fall into the range between 113 and 137  $\mu\text{m}$ . Note that this critical radius, where movement of the cargo is expected to stall, is an averaged

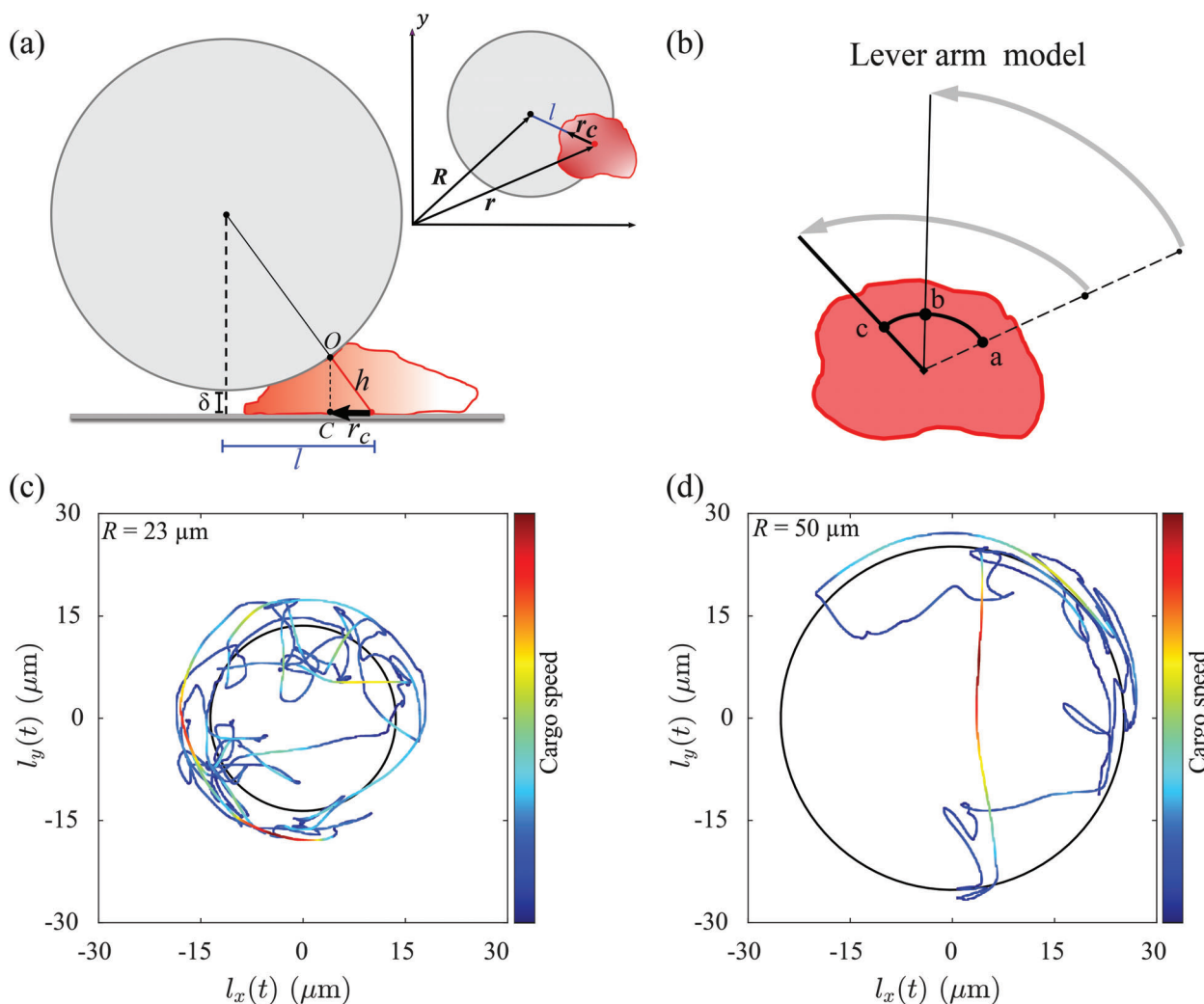


**Figure 4.** Geometry of the system and the lever arm model. a) Cross-section (side view) of the cell–cargo system, exclusive to episodes of the idling state when the particle is in contact with the substrate. The cell is shown in red and the cargo in gray. The distance between the cell and the cargo centers of mass on the cell–substrate contact plane is denoted by  $l$ ; the cargo radius is  $R$ , and  $\delta$  is the average height of the particle surface above the substrate (here taken to be equal to  $5\ \mu\text{m}$ ). We denote further  $O$  as the point where the line that connects the center of mass of the cell–substrate contact area with the center of the spherical cargo particle intersects the cargo surface. The projection of this point on the substrate defines the contact point,  $C$ , with  $r_c$  describing its position vector with respect to the cell. The top view of the system is shown in the figure inset, confer Figure 1b. b) The lever arm model: The diagram explains the displacement of the cargo at the level of the cell–cargo contact point. The cartoon compares the displacement of two particles of different sizes in the laboratory frame within a fixed time interval. The larger particle tends to be further away from the cell [larger equilibrium distance  $l_0$ , cf. Equation (3)]. The two gray arcs have the same length— however, the cell–cargo contact point at the level of the cell has moved a smaller distance [from (a) to (b)] to displace the larger cargo in comparison to the smaller cargo, where the contact point has moved from a to c within the same time interval in order to achieve equal cargo displacements. In short, the speed of the cell–cargo contact point decreases as a function of the radius  $R$  but the recorded colloid speed in the lab frame remains unchanged. c,d) The cargo trajectories are shown in the frame of reference of the cell for a particle with  $R = 23\ \mu\text{m}$  and  $R = 50\ \mu\text{m}$ , respectively; the color-code represent the magnitude of the cargo speed from blue (lowest) to red (highest). The solid black circle marks the equilibrium distance.

quantity. Due to cell to cell variability, this limit may vary considerably between individual cells.

## 2.6. Estimate of Cargo Speed and Active Force beyond the Experimentally Accessible Regime

Having determined the full range of cargo sizes that can be moved by an amoeboid carrier cell, we can now estimate the cargo

speeds and the active forces from the contact point speed also for larger cargoes outside the experimentally accessible range. For this purpose, we use the established relation of the measured cargo dynamics  $R(t)$  and the contact point  $r_c(t)$  via Equations (1) and (2); as argued before, the cell speed can approximately be neglected—the cell is considered non-motile at the timescales of interest. Note that for cargo sizes outside the regime that we can analyze in our experiments, the time series  $l(t)$  of the cell–cargo distance is no longer available. That is why we approximate  $l(t)$

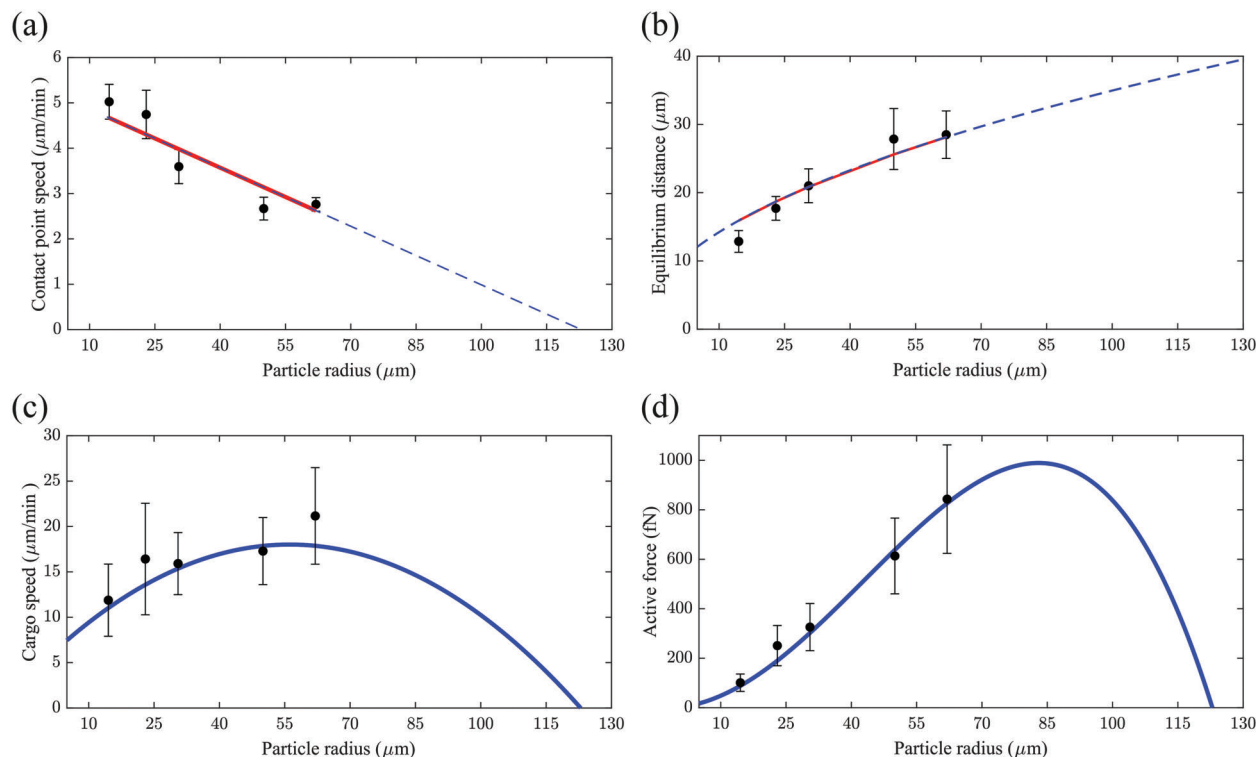


**Figure 5.** Results of the geometrical model. a) The descending contact point speed as a function of cargo radius. For each particle size, the black data points represent the median of the contact point speeds. The error bars are the standard error of the mean ( $2\sigma$  interval); see Figure S4, Supporting Information for details of the contact point speed statistics. The red solid line shows a linear fit to the data points. The particle radius at which the contact point reaches zero values is  $123\ \mu\text{m}$  ( $1\sigma$ -confidence interval:  $[113\ \mu\text{m}, 137\ \mu\text{m}]$ , estimated from the uncertainties of the inferred fit parameters). b) The mean equilibrium distance  $l_0$  (black points) and the nonlinear fit to the measured data (red solid line) using Equation (3). c) The speed of the cargo estimated for the full range of particle sizes. For each particle size, the black points are the mean cargo speeds derived from isolated idling states of all trajectories. The solid blue line is the mean cargo speed predicted by the geometrical model. d) Using the cargo speeds from the geometrical model, the mean active force is estimated for the full range of particle sizes. The black points are data of mean active forces (identical to Figure 3). The solid blue line with a peak force at  $\approx 400\ \text{nN}$  is the mean active force estimated from the geometrical model. The error bars of the data points in panels (b) to (d) represent standard deviations.

in Equations (1) and (2) by the equilibrium distance  $l_0 = l_0(R)$ , which depends on the cargo radius. For the experimentally accessible cargo sizes, the equilibrium distance  $l_0$  increases with increasing cargo radius  $R$ , see Figure 5b. We fit the dependence of  $l_0$  on  $R$  using the model function

$$l_0(R) = \sqrt{(h + R)^2 - (R + \delta)^2} \quad (3)$$

which was inspired by the geometry of the system, confer the right-angled triangle in Figure 4a with hypotenuse length  $h + R$  and the legs  $\{R + \delta, l_0\}$ . Note that this fit to the experimental data yields an estimate of  $h = 10.6\ \mu\text{m}$ , which is a reasonable number given the typical dimensions of a *D. discoideum* cell.<sup>[32,33]</sup>

Extrapolating the contact point speed (Figure 5a) and the fit function [Equation (3)] to larger cargo radii (Figure 5b), we obtain estimates of the average cargo speeds by differentiating Equation (1) with respect to time. In Figure 5c, the resulting cargo speeds are displayed as a function of the radius  $R$  (blue line). For smaller cargo sizes, the speed increases and reaches a maximum of  $18\ \mu\text{m}\ \text{min}^{-1}$  for cargo radii of  $\approx 55\ \mu\text{m}$ . Toward larger sizes, the speed then decreases and drops to zero at the critical radius of

$123\ \mu\text{m}$ . This is in good agreement with the experimentally measured speeds during the rest phase, displayed as black data points in Figure 5c. The data, however, shows strong fluctuations and is limited to sizes up to a radius of  $62\ \mu\text{m}$ . The speeds of larger cargoes are only accessible based on the proposed geometrical lever arm model.

Finally, we also estimated the corresponding active forces according to Stokes' law based on measurements of the cargo speeds. As shown in Figure 5d, the force increases for smaller radii and goes through a maximum, before dropping to zero at the limiting cargo radius of  $123\ \mu\text{m}$ . The peak value of  $1\ \text{pN}$  is reached for a particle radius of  $83\ \mu\text{m}$ . As already indicated above, this maximum is an average value. Depending on the individual cell, peak force of  $\approx 3\ \text{pN}$  can be observed over short periods of time (Figure 3b).

## 2.7. Cell–Cargo Interaction under a Constant External Pulling Force

So far, we have focused on amoeboid microtransport on an open flat substrate in a uniform viscous fluid medium at rest.

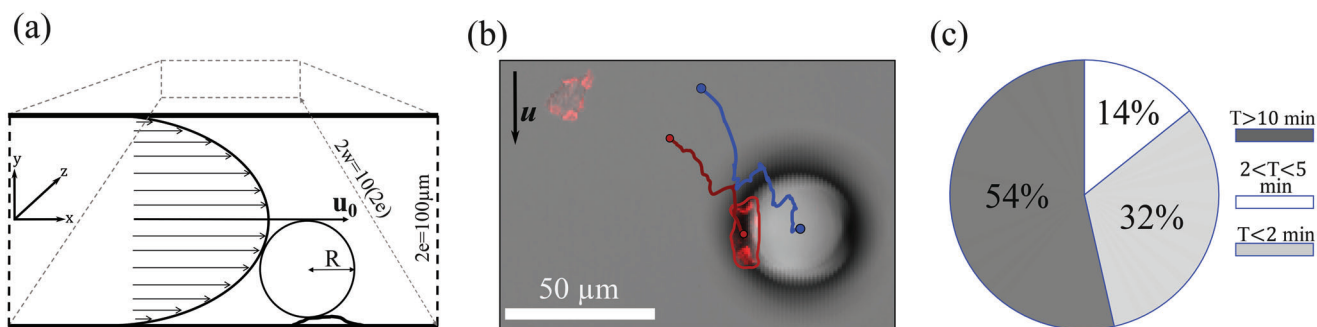


**Figure 6.** Cell–cargo system under a constant drag force. a) Cross-section of the micro-channel including main geometrical quantities and the parabolic flow profile;  $u_0$  is the maximum flow speed at the center of the channel (geometry:  $e = 50 \mu\text{m}$ ,  $w = 0.5 \text{ mm}$ ). The cell is in contact with a particle of radius  $23 \mu\text{m}$ , covering up to the half-height of the channel. b) A microscope image of the cell (red) and cargo (gray sphere) under flow conditions. The tracks of the cell (in red) and the cargo (in blue) show the displacement of the entire system downstream (Movie S9, Supporting Information). The black arrow shows the direction of the flow. c) The pie chart characterizes the total percentage of the loaded cells under the critical flow that withhold to the cargo over 10 min (54%,  $n = 15$ ), between 2 to 5 min (14%,  $n = 4$ ), or lose the cargo shortly after the flow insertion (32%,  $n = 9$ ). The flow rate is  $3 \mu\text{L min}^{-1}$ .

However, a carrier cell will typically experience more complex environments, where friction forces due to geometrical confinement or fluid flow may additionally affect the cargo particle. As biological cells including *D. discoideum* are mechanoresponsive,<sup>[34–36]</sup> we expect that the active forces exerted by the carrier cell may change if additional external forces are acting on the cargo particle. To provide a first estimate of how external conditions may affect the force generation of the carrier cell, we exposed amoebae that were loaded with a spherical cargo particle to a constant drag force generated by fluid flow in a microfluidic device, see **Figure 6a,b** and Movie S9, Supporting Information.

A schematic of the rectangular flow chamber with half height  $e$  and half width  $w$  (much larger than the height:  $w \gg e$ ) is depicted in **Figure 6a**. Since the Reynolds number is low, inertial effects can be neglected. The flow between parallel plates then exhibits a parabolic profile,

$$u(y) = u_0 \left( 1 - \frac{y^2}{e^2} \right) \quad \text{with} \quad u_0 = \frac{dp}{dx} \times \frac{e^2}{2\eta} \quad (4)$$

where  $u_0$  is the flow speed at the center of the channel,  $\eta$  is the viscosity of the medium (here, taken to be equal to the viscosity of water at  $20 \text{ }^\circ\text{C}$ ) and  $dp/dx$  is the pressure gradient along the length of the channel.<sup>[37,38]</sup> In our experiments, we used particles with a radius of  $23 \mu\text{m}$ . We gradually increased the flow rate and thereby the drag force on the cargo particle to the point where about half of the cells lost their cargo, indicating that we approached the critical force required to rupture the adhesive bond between the cell and the cargo particle. At a flow rate of  $3 \mu\text{L min}^{-1}$ —corresponding to a peak velocity of  $0.75 \text{ mm s}^{-1}$  and a pressure gradient of  $0.6 \text{ Pa mm}^{-1}$ —we observed that 54% ( $n = 15$ ) of the cells maintained their adhesion to the cargo particle, while the remaining 46% ( $n = 13$ ) lost connection to the cargo either immediately or within 5 min after starting the fluid flow (cf. **Figure 6c**).

To ensure that the observed effects are only due to the drag force acting on the cargo particle, the wall shear stress should remain below the critical value of  $0.8 \text{ Pa}$  above which *D. discoideum*

cells start exhibiting shear induced directional responses.<sup>[36,39,40]</sup> For the critical flow rate of  $3 \mu\text{L min}^{-1}$ , the wall shear stress is  $30 \text{ mPa}$ , remaining indeed below the threshold value of  $0.8 \text{ Pa}$ . Consequently, comparing the tracks of single cells without cargo in stationary liquid (blue tracks) and under flow (red tracks), no directional movement was detected, see **Figure 7a,d**. Only a moderately enhanced but isotropic spreading was observed in the presence of fluid shear stress.

In contrast, a clear directional bias was observed in the presence of a fluid flow for cells that carry a cargo particle, see **Figure 6b** for an example: the entire cell–cargo system was pulled downstream as a consequence of the drag force acting on the cargo particle (see **Figure 7e** for several examples of cargo trajectories under fluid flow). Cargoes in the absence of fluid flow, on the other hand, spread isotropically, as shown in **Figure 7b**. Moreover, we found that the cargo particle is oriented exclusively in downstream direction with respect to the cell under fluid flow, see the red arrows in **Figure 7f**, while the cell can position the cargo in any direction at its periphery in the isotropic environment of a resting fluid, see the blue arrows in **Figure 7c**.

In the microfluidic setup, the cargo radius is comparable to the channel height. Taking into account the top and bottom channel boundaries, the hydrodynamic drag force  $F$  acting on the cargo particle is not exactly following Stokes' law. Similar to our analysis of the cell–cargo system near a flat surface, here we also assume that, due to the presence of the cell, the cargo stays on average  $5 \mu\text{m}$  away from the bottom surface of the channel. Based on the solution presented in refs. [31, 41, 42], we find that a particle with a radius of  $23 \mu\text{m}$  in a Poiseuille flow (with  $u_0 = 0.75 \text{ mm s}^{-1}$  at the channel's center) experiences a drag force of  $\approx 0.5 \text{ nN}$ .

### 3. Discussion and Conclusion

Here, we explored the active forces involved in cell-driven micro-transport by monitoring the movement of spherical cargo particles and estimated the corresponding drag forces that act on the cargo particles based on their speed in an isotropic viscous fluid environment. The cargo speed remained approximately constant for all tested particle sizes except for the smallest particles of

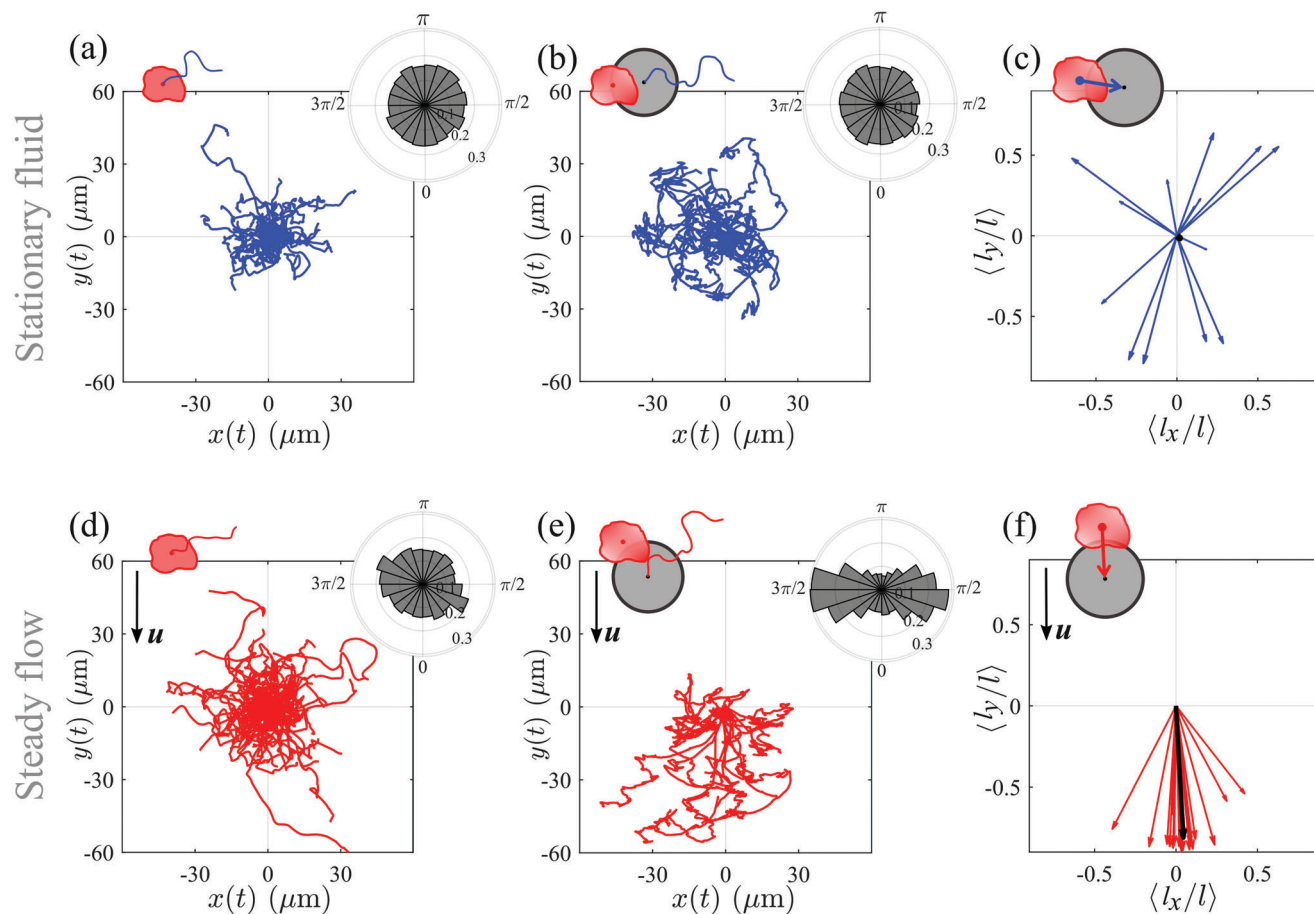


**Figure 7.** Dynamics of unloaded cells and cell–cargo system under flow conditions. a) The trajectories of single cells ( $n = 77$ ) and b) the trajectories of cargoes ( $n = 15$ ) are shown from a common origin in the absence of flow. d) The trajectories of single cells ( $n = 104$ ) and e) the trajectories of cargoes ( $n = 15$ ) are shown from a common origin under a Poiseuille flow (flow rate of  $3 \mu\text{L min}^{-1}$ ). Individual cells show no sign of directional motion in both, stationary and flow conditions. In contrast, the entire cell–cargo system tends to move downstream on average under flow conditions as shown in (e). The polar plots in (a,b) and (d,e) show the angle between the respective velocity vector and the flow direction. The polar plot (e) suggests that the cell displaces the cargo mainly perpendicular to the flow direction. The arrows in panels (c) and (f) show the mean of the normalized displacement vector  $l/l$ , where  $l = R - r$ , that is, the cargo position with respect to the cell for a stationary fluid (c) and under flow (f); the overlaid black arrow is the average. Whereas a cell can place the cargo at arbitrary positions in the absence of flow, the particle tends to be placed downstream under flow conditions.

radius  $R = 14.5 \mu\text{m}$ , where lower speeds were observed. This is in line with a lever arm model based on the geometry of the system. Another reason for a decreased speed for smaller particles could be the phagocytic capacity of *D. discoideum* cells:<sup>[29,43,44]</sup> while the curvature of larger particles is not sufficient to trigger phagocytosis, particles with a radius of  $14.5 \mu\text{m}$  may be small enough to stimulate attempts, albeit unsuccessful, to engulf the particles, resulting in reduced pseudopod formation, motility, and cargo transport. The similar speeds for larger particle sizes imply that cells generate active forces that increase with particle size, resulting in averaged forces up to  $0.95 \text{ pN}$  that were observed in our experiments.

We see two potential reasons for this unexpected dependence of the active forces on the cargo size. First, larger particles experience larger drag forces and, thus, resist the cell-driven movements more strongly than smaller particles. The forces that drive the particle motion are, however, generated by the actin cytoskeleton inside the carrier cell, which has mechanosensitive and adaptive properties. The active forces that arise from the cytoskeletal

activity may thus depend on the external drag in a nonlinear fashion. This is supported by earlier measurements of force–velocity relations at the leading edge of protruding lamellipodia, where it was observed that the speed of movement does not show a linear decrease with increasing opposing force. Instead, nonlinear relations were observed, where the velocity may even transiently increase for larger loads,<sup>[45,46]</sup> similar to our observations in Figure 5d. Second, the cellular microenvironment, in particular the degree of confinement, may strongly affect the cellular response.<sup>[27,34,35,47–52]</sup> In our cargo-transport situation, the cell is confined between the substrate and the surface of the cargo particle, so that particles of different radii expose the cells to geometrically different confinements and, thus, different mechanical stimuli. This may trigger different confinement-induced responses, resulting in elevated active forces for larger cargo particles. Indeed, we observed that cargo-loaded cells disperse at a faster rate compared to cargo-free cells, see Figure S5, Supporting Information, suggesting that the presence of the cargo influences cell motility and potentially enhances the spreading

dynamics of the cargo-loaded cells. Note, however, that the speed of the cargo particle is not directly related to the speed of the carrier cell but additionally affected by shape changes and cytoskeletal activity at the dorsal cell cortex.

Even though we did not observe a decreasing cargo speed for larger particles, transport will eventually stall for very large cargo sizes, as the active forces that a single cell can generate must be limited. Unfortunately, this regime is not accessible in our experimental setting. For larger particle sizes, it becomes increasingly difficult to ensure that only one carrier cell is in contact with the cargo. Moreover, it is difficult to decide whether a cell–cargo contact is actually established or not for large particles that are hardly displaced by single cells (see Movie S10, Supporting Information for an exemplary case featuring a large particle with a radius of 107  $\mu\text{m}$ , where cargo transport has practically stalled). Given that we need a sufficient number of cargo trajectories to reliably estimate the speed and drag force on the cargo particle, data on cargo sizes beyond a radius of  $R = 62 \mu\text{m}$  was not accessible in our experiments. To close this gap, we proposed a simple geometrical model to estimate the position and speed of the cell–cargo contact point. Together with our experimental data, this model shows that the speed of the contact point decreases with increasing particle size, allowing us to extrapolate toward larger cargoes and to estimate the critical cargo size, where cell-driven transport finally stalls. Based on this approach, we predict that single motile *D. discoideum* cells can move spherical particles up to radii of  $\approx 123 \mu\text{m}$ . Note that thermal diffusion of the cargo particles can be neglected in our experiments due to the much stronger adhesion forces between the cells and the cargo particles (for comparison, the average displacement of a freely diffusing particle of radius  $R = 50 \mu\text{m}$  over a measurement time of 10 min due to thermal diffusion would be 5  $\mu\text{m}$ , while cargo particles that are randomly displaced by carrier cells move 32  $\mu\text{m}$  on average within the same time).

Note that the maximum forces we observed did not exceed averaged values of 0.95 pN. Also the forces predicted by our model for larger particle sizes beyond the experimentally accessible regime do not reach values larger than 1 pN. Compared to other forces that are observed on the cellular scale, such as adhesion forces, cell–substrate traction forces, or even forces exerted by single molecular motors, these are very small values.<sup>[24,46,49,53–55]</sup> We thus conclude that it is not the Stokesian friction that imposes a size limit on the cargo particles that can be transported by single amoeboid cells. Instead, we conjecture that the decreasing speed of the cell–cargo contact point may have geometrical reasons. For small cargo radii the cell will experience a wedge-shaped confinement that stimulates and guides its migration in an attempt to maximize contact to available surfaces,<sup>[56]</sup> including intermittent bursts of polarization in the direction of the cargo particle.<sup>[15]</sup> With increasing particle radius, the difference in slope between the confining bottom and top surfaces will become less and less pronounced, resulting in less frequent polarity bursts, see Figure 1f, and a decreasing overall transport activity that is reflected by a decay of the cell–cargo contact point speed, see Figure 5a.

The behavior of cargo loaded cells under fluid flow, resulting in constant drag forces as high as 0.5 nN, is supporting our interpretation. In our experiment, half of the population of cells carrying particles with a radius of 23  $\mu\text{m}$  could resist this drag

force for over 10 min. In particular, among the cargo trajectories of this population that were mostly drifting downstream, we also observed short episodes, where the cargo was moved against the flow-induced drag force of 0.5 nN, see Movies S11 and S12, Supporting Information for examples of short upstream excursions of the cargo displacement. This is confirmed by the distribution of cargo displacements along the flow direction as shown in Figure S6, Supporting Information, where a substantial fraction of upstream displacements against the drag force of the fluid flow can be seen. It shows that, instead of merely acting as a glue that connects the cargo to the substrate, the cell can also actively displace the cargo against the flow and may thus generate forces that, at least shortly (for time intervals on the order of seconds), exceed the hydrodynamic friction forces that arise when moving the cargo in a liquid at rest by three orders of magnitude. We assume that these peak forces are triggered in response to the mechanical stimulus the cell experiences when the fluid flow is pulling the cargo particle, a persistent mechanical cue that is absent in a fluid at rest, where only much smaller forces were observed. This is in line with earlier modeling work that has suggested that a catch bond mechanism may be involved in the evolution of cell–substrate forces during *D. discoideum* locomotion.<sup>[52,54]</sup> In particular, mechanosensitive interactions were identified as the key factor to trigger periodic length change during amoeboid migration. We thus hypothesize that, also in our case, a similar mechanism underlies the repeated contractions causing the brief episodes of increased pulling forces on the cargo in the presence of a flow. For larger flow speeds, the resulting drag force will exceed the average cell–cargo adhesion force and detach the cargo particle from the cell in most cases. The cell–cargo adhesion strength estimated from the persistent drag force on the cargo attached to a cell is two- to fourfold smaller than the known cell adhesion forces to a glass substrate.<sup>[24,57]</sup> This is in line with our experimental observation that cells remain attached to the substrate even after losing the cargo.

To conclude, we showed that single amoeboid cells are capable of transporting cargo particles significantly larger than their own body size exerting minuscule forces in the sub-piconewton range. These forces can increase by several orders of magnitude if an external counter force is actively pulling on the cargo particle. Our findings highlight the potentials and limits of amoeboid cells for designing autonomous biohybrid transport systems and for studying future applications of these systems when operating under more complex, real world conditions. As amoeboid motility is common to many mammalian cell types, our findings will be relevant for putting biohybrid transport in medical applications into practice.

## 4. Experimental Section

**Cell Culturing:** LifeAct-mRFP AX2 axenic *D. discoideum* mutant cells were cultivated in tissue culture flasks (TC Flask T75 Standard, Sarstedt AG & Co. KG, Nümbrecht, Germany) in a nutrient medium (HL5 medium including glucose supplemented with vitamins and micro-elements, Formedium Ltd., Norfolk, England) at 20 °C. The medium was supplemented with a penicillin (final concentration: 100 I.U.mL<sup>-1</sup>) and streptomycin (final concentration: 100  $\mu\text{g mL}^{-1}$ ) antibiotics mix (CELLPURE Pen/Strep-PreMix, Carl Roth GmbH+Co. KG, Karlsruhe, Germany) and

G418 (G418 disulfate ultrapure, VWR International, LLC.) as selection agent (final concentration of  $10 \mu\text{g mL}^{-1}$ ). Prior to the first harvest of the cells, the spores were grown adherently to the glass bottom dish for 4 up to 7 days followed by a renewal of the medium every second day. After reaching over 50% confluent monolayer, the cell suspension was diluted (ratio 1:200 of cell vs. medium) at each medium renewal to avoid over-confluency. In addition, the entire cell culture was renewed every 4 weeks to avoid the accumulation of any undesired mutation arising from genetic drift.

**Sample Preparation:** Monodispersed spherical particles (microParticles GmbH, Berlin, Germany) with a diameter range between 10 to  $214 \mu\text{m}$  were stored in deionized water at  $4-7^\circ\text{C}$ . Prior to the experiment, cells were harvested from the cell culture flask. The cell suspension was then diluted to obtain a cell count of roughly  $5 \times 10^4$  cells  $\text{mL}^{-1}$  for experiments with particles of up to  $75 \mu\text{m}$  and  $3 \times 10^4$  cells  $\text{mL}^{-1}$  for larger particle sizes.  $1.5 \text{ mL}$  of the cell suspension was then transferred into a culture dish (FluoroDish™ tissue culture dish with a cover glass bottom –  $35 \text{ mm}$ , World Precision Instruments, Inc., Sarasota, Florida, USA). Cells sedimented and adhered to the bottom of the dish within 15 min. Afterward,  $8-15 \mu\text{L}$  of the particle suspension was added to the sample to achieve an approximate particle–cell ratio of 1:5. The sample was then gently shaken to achieve a uniform particle distribution. Before the imaging, the sample was kept at rest for another period of 15 min.

For microfluidic experiments, glass bottom channels with rectangular cross sections were used, purchased from ibidi ( $\mu\text{-slide VI 0.1: 0.1 mm}$  height,  $1 \text{ mm}$  width, ibidi GmbH, Martinsried, Germany). First, the channel was filled with  $1.7 \mu\text{L}$  of cell suspension containing  $2 \times 10^6$  cells  $\text{mL}^{-1}$ . The sample was kept at rest for 15 min to ensure cell–substrate adhesion. Next, a few droplets of the dense particle suspension was added to the channel inlet. A  $1 \text{ mL}$  gas-tight microsyringe (Harvard Apparatus, Holliston, USA) was filled with cell culture medium and mounted on a PHD Ultra micropump (Harvard Apparatus, Holliston, USA), then gently connected to the channel inlet via PTFE tubing (FEP Tubing,  $1/16$  inch outside diameter,  $0.03$  inch inside diameter, IDEX HEALTH & SCIENCE, USA). The small pressure resulting from connecting the tubes to the channel inlet was sufficient to push the particles into the channel. Accumulated cells and particles in the channel inlet as well as any trapped air bubbles were then removed by applying a gentle flow. The sample with all connected tubes was kept at rest for further 30 min to reach a stationary state. Subsequently, the medium was injected into the channel at a constant flow rate of  $3 \mu\text{L min}^{-1}$ .

For chemotaxis experiments LifeAct-mRFP AX2 axenic *D. discoideum* mutant cells were washed and starved in phosphate buffer (including  $14.6 \text{ mM}$   $\text{KH}_2\text{PO}_4$  and  $2 \text{ mM}$   $\text{Na}_2\text{HPO}_4$ ,  $\text{pH} = 6$ , Merck, KGaA, Darmstadt, Germany) for 3 to 4 h prior to the experiments. The cell suspension was then transferred to a culture dish (FluoroDish™ tissue culture dish with a cover glass bottom –  $35 \text{ mm}$ , World Precision Instruments, Inc., Sarasota, Florida, USA) and rested for  $\approx 15$  min to ensure cell–substrate adhesion. Afterward, the buffer was replaced with nutrient medium, HL5, and the sample was rested for another 15 min. The chemo-attractant point source was established using a glass micropipette (opening diameter  $0.5 \mu\text{m}$ , Eppendorf AG, Hamburg, Germany) releasing  $100 \text{ mM}$  cyclic adenosine monophosphate (cAMP) through diffusion close to the substrate. The micropipette was assembled on a micro-manipulator (PatchMan NP2, Eppendorf AG, Hamburg, Germany) which was used to manipulate the dynamic and static positioning of the chemo-attractant point source.

**Imaging:** Imaging was performed using confocal laser scanning microscopy (LSM 780, Zeiss, Oberkochen, Germany). The fluorophore mRFP, colocalized with the F-actin of the cytoskeleton of cells, was excited with a  $561 \text{ nm}$  laser for cell detection (pinhole aperture of 1 Airy unit,  $40\times/64\times$  objectives). The emitted light was band-pass filtered between  $585-727 \text{ nm}$  and collected by a photo-multiplier. The full spectrum transmitted light was also collected using a second acquisition channel where the bright-field images were generated as a result of discontinuous refractive indices. These images were then used for particle detection. The focal plane was adjusted to the height where the ventral surface of the cell meets the substrate and the lower section of the particles appeared as a bright spot surrounded by a dark ring. Images were acquired with a

sampling time (time interval) of  $\Delta t = 0.197 \text{ s}$ . Individual cell–cargo interactions were recorded as long as possible, with a maximum of 2 h; the measurement time was limited by interruptions, such as collisions with neighboring particles, cell division or the interference with another cell.

For experiments in microfluidic channels, the sample was imaged at a frame rate of 2 fpm as long as the cargo remained attached to the cell (up to 40 min). The recording was stopped or discarded if floating cells bound to the cell–particle configuration of interest or if other interruptions occurred (cf. discussion above).

**Image Analysis:** The image processing was performed using custom algorithms written in Matlab (R2021b, MathWorks, Natick, MA, USA).

Cell and particle segmentation was based on the images from the fluorescent channel collecting the emission signals of the labeled F-actin and the bright-field channel that collects the transmitted light, respectively. The image sequence was initially subjected to noise reduction using median filtering, followed by contrast enhancement protocols including a sequence of nonlinear histogram remappings. Subsequently, a threshold determined by the Otsu method<sup>[58]</sup> was applied to the preprocessed images for binarization. The binarized images were then segmented followed by tracking of the resultant objects<sup>[59]</sup> based on the center of mass of segmented regions. In the case of cells, segmented boundaries were beforehand processed with an active contouring algorithm;<sup>[60–62]</sup> the resulting boundaries were used to determine the cell's center of mass. Note that the cell and the cargo positions were defined as the 2D center of mass coordinates, derived from the connected components of binarized images.

**Data Analysis:** The complete statistical analysis was performed in Matlab (R2021b, MathWorks, Natick, MA, USA).

To avoid spurious fluctuations of the velocities due to the collected noise during high-frequency scanning, both the cell and the cargo trajectories were smoothed before data analysis by applying a moving average to each trajectory independently. To ensure that the major dynamics of the trajectories were captured also after smoothing, the length of the smoothing window was set equal to the decay time of the velocity correlation function of that trajectory, estimated as summarized in the following. Let the coordinates of the segmented object (cell or cargo) in frame  $i$  be denoted by  $\mathbf{X}_i = \mathbf{x}_i + \sigma_i$ , where  $\mathbf{x}_i$  is the true position of the object and  $\sigma_i$  denotes the imaging noise. The imaging errors in frames  $i$  and  $j$  are unbiased and uncorrelated

$$\langle \sigma_i \rangle = 0, \quad \langle \sigma_{i,\mu} \sigma_{j,\alpha} \rangle = s^2 \delta_{i,j} \delta_{\alpha,\mu} \quad (5)$$

where  $s^2$  is the variance of the error from object tracking and  $\sigma_{i,\mu}$  denotes the  $\mu$ th Cartesian component of the noise in frame  $i$ . Therefore, the  $i$ th measured velocity reads  $\mathbf{V}_i = (\mathbf{X}_{i+1} - \mathbf{X}_i) / \Delta t = \mathbf{v}_i + \boldsymbol{\eta}_i$ , where  $\Delta t$  denotes the time step,  $\mathbf{v}_i$  is the true secant velocity and  $\boldsymbol{\eta}_i$  is the error of velocity  $\mathbf{V}_i$ . The properties of the imaging noise [Equation (5)] imply

$$\langle \boldsymbol{\eta}_i \rangle = 0 \quad (6a)$$

$$\langle \eta_{i,\mu} \eta_{j,\alpha} \rangle = \frac{s^2}{\Delta t^2} \delta_{\mu,\alpha} [2\delta_{i,j} - \delta_{i+1,j} - \delta_{i,j+1}] \quad (6b)$$

Using these definitions, the expectation value of the empirical velocity auto-correlation function for a trajectory with a total number of  $N$  frames can be written as follows

$$\begin{aligned} \langle C_\Delta \rangle &= \frac{1}{N - \Delta} \sum_{i=1}^{N-\Delta} \langle \mathbf{V}_i \cdot \mathbf{V}_{i+\Delta} \rangle \\ &= \tilde{C}_\Delta + \frac{2s^2}{\Delta t^2} (2\delta_{\Delta,0} - \delta_{\Delta,1} - \delta_{\Delta,-1}) \end{aligned} \quad (7)$$

where  $\tilde{C}_\Delta = \sum_{i=1}^{N-\Delta} \mathbf{v}_i \cdot \mathbf{v}_{i+\Delta} / (N - \Delta)$  for  $\Delta = 0, 1, 2, \dots, N - 1$  is the true velocity auto-correlation function. Accordingly, the empirical auto-correlation function of the noisy secant velocities  $\mathbf{V}_i$  is an unbiased estimator of the correlation function of  $\mathbf{v}_i$  for  $\Delta \geq 2$ , since imaging noise

does only affect the first two values  $\tilde{C}_{\Delta=0}$  and  $\tilde{C}_{\Delta=1}$ . We fitted an exponentially decaying function to the first 100 points of the velocity correlation function for  $\Delta \geq 2$  and extrapolated for  $\Delta = 0$  and  $\Delta = 1$ . The length of the smoothing window was chosen to be equal to the decay time  $\tau_c$  of the fitted exponential, proportional to  $e^{-t/\tau_c}$ . For an example of the velocity correlation function and the exponential fit, both for the cell and the cargo, see Figure S2, Supporting Information. Depending on the trajectory, the length of the smoothing window varies from 10 to 30 s for the cell and 5 to 10 s for the cargo trajectories, respectively.

The polarization rate  $\lambda$  was calculated as follows. Initially, the time series of cell–cargo relative distance  $l(t) = |\mathbf{R}(t) - \mathbf{r}(t)|$  was standardized by subtracting its time-wise mean  $\overline{l(t)}$  and then dividing by the standard deviation for that recording session. The histograms were accumulated across the entire population, which showed a skewed distribution. For every particle size the distributions were fitted to a double Gaussian function. The skewness in the distributions [see Figure 1e for an example] is largely attributed to the notable reductions in the distance  $l(t)$  from the preferred value  $l_0$ , reflecting moments of transition between the “idling” and “dynamic” phases.

For all groups of particle sizes, a deviation of the distance  $l(t)$  toward zero by more than 1.75-times the standard deviation from its mean indicated a transition and was therefore selected as a reliable threshold. Finally, the transitions were counted by converting the time series into a binary format according to the threshold.

Assuming that the polarization rate is Poisson-distributed, the probability of observing  $k$  polarization instances within a time span  $\tau$  is

$$P_{\tau}(k|\lambda) = \frac{(\lambda\tau)^k e^{-\lambda\tau}}{k!} \quad (8)$$

leading to the likelihood function

$$\mathcal{L} = \prod_{i=1}^N P_{\tau_i}(k_i|\lambda) \quad (9)$$

For each particle size, we observed  $N \approx 10$  independent recordings of length  $\tau_i$  and counted the number of polarization events  $k_i$  ( $i = 1, 2, \dots, N$ ). The maximum-likelihood prediction  $\hat{\lambda}$  for the rate  $\lambda$  was computed as the cumulative count of recorded instances divided by the overall time of observation

$$\hat{\lambda} = \frac{\sum_{i=1}^N k_i}{\sum_{j=1}^N \tau_j} \quad (10)$$

Close to its peak value, the likelihood is considered Gaussian with mean  $\hat{\lambda}$  and standard deviation  $\sigma_{\lambda}$

$$\sigma_{\lambda} = \frac{\hat{\lambda}}{\sqrt{\sum_{j=1}^N k_j}} \quad (11)$$

The  $1\sigma$ -range is reflected in the error bars in Figure 1e.

All regressions shown in the main text (Figures 1f, 5b,c) were performed by minimizing the reduced chi-square statistics (mean squared weighted deviation).

## Supporting Information

Supporting Information is available from the Wiley Online Library or from the author.

## Acknowledgements

S.S.P. and C.B. gratefully acknowledge funding by Deutsche Forschungsgemeinschaft (DFG) via project *Sachbeihilfe* BE 3978/3-3. V.L. and C.B. ac-

knowledge financial support via the IMPRS *Multiscale Bio-Systems*. The authors thank Vedrana Filić, Maja Marinović, and Igor Weber (Rudjer Boskovic Institute, Zagreb, Croatia) for providing the Lifeact-mRFP encoding plasmid, and Kirsten Sachse as well as Maike Stange for technical support.

Open access funding enabled and organized by Projekt DEAL.

## Conflict of Interest

The authors declare no conflict of interest.

## Author Contributions

S.S.P. conducted experimental research. V.L. contributed experimental data. R.G. contributed to the modeling. S.S.P. and C.B. wrote the manuscript. R.G. and V.L. commented on the draft. C.B. designed and supervised the project.

## Data Availability Statement

The data that support the findings of this study are available from the corresponding author upon reasonable request.

## Keywords

active microtransport, amoeboid motion, biohybrid systems, cell migration forces, mechanosensing

Received: June 2, 2023  
Revised: September 12, 2023  
Published online:

- [1] J. Katuri, X. Ma, M. M. Stanton, S. Sánchez, *Acc. Chem. Res.* **2016**, *50*, 2.
- [2] M. Sitti, *Nature* **2009**, *458*, 1121.
- [3] M. B. Akolpoglu, Y. Alapan, N. O. Dogan, S. F. Baltaci, O. Yasa, G. A. Tural, M. Sitti, *Sci. Adv.* **2022**, *8*, eabo6163.
- [4] C. Jin, Y. Chen, C. C. Maass, A. J. T. M. Mathijssen, *Phys. Rev. Lett.* **2021**, *127*, 088006.
- [5] H. Xu, M. Medina-Sánchez, V. Magdanz, L. Schwarz, F. Hebenstreit, O. G. Schmidt, *ACS Nano* **2017**, *12*, 327.
- [6] B.-W. Park, J. Zhuang, O. Yasa, M. Sitti, *ACS Nano* **2017**, *11*, 8910.
- [7] A. Sokolov, M. M. Apodaca, B. A. Grzybowski, I. S. Aranson, *Proc. Natl. Acad. Sci. USA* **2009**, *107*, 969.
- [8] R. Ahmad, A. J. Bae, Y.-J. Su, S. G. Pozveh, E. Bodenschatz, A. Pumir, A. Gholami, *Soft Matter* **2022**, *18*, 4767.
- [9] R. D. Leonardo, L. Angelani, D. Dell'Arciprete, G. Ruocco, V. Iebba, S. Schippa, M. P. Conte, F. Mecarini, F. D. Angelis, E. D. Fabrizio, *Proc. Natl. Acad. Sci. USA* **2010**, *107*, 9541.
- [10] N. Doshi, A. J. Swiston, J. B. Gilbert, M. L. Alcaraz, R. E. Cohen, M. F. Rubner, S. Mitragotri, *Adv. Mater.* **2011**, *23*, H105.
- [11] Y. Wu, X. Dong, J. Kim, C. Wang, M. Sitti, *Sci. Adv.* **2022**, *8*, eabn3431.
- [12] H. Lu, M. Zhang, Y. Yang, Q. Huang, T. Fukuda, Z. Wang, Y. Shen, *Nat. Commun.* **2018**, *9*, 3944.
- [13] W. Hu, G. Z. Lum, M. Mastrangeli, M. Sitti, *Nature* **2018**, *554*, 81.
- [14] O. Nagel, M. Frey, M. Gerhardt, C. Beta, *Adv. Sci.* **2018**, *6*, 1801242.
- [15] V. Lepro, R. Großmann, S. Sharifi Panah, O. Nagel, S. Klumpp, R. Lipowsky, C. Beta, *Phys. Rev. Appl.* **2022**, *18*, 034014.

- [16] W. Wang, W. Duan, S. Ahmed, T. E. Mallouk, A. Sen, *Nano Today* **2013**, *8*, 531.
- [17] R. W. Carlsen, M. Sitti, *Small* **2014**, *10*, 3831.
- [18] L. Sun, Y. Yu, Z. Chen, F. Bian, F. Ye, L. Sun, Y. Zhao, *Chem. Soc. Rev.* **2020**, *49*, 4043.
- [19] H. Ceylan, I. C. Yasa, O. Yasa, A. F. Tabak, J. Giltinan, M. Sitti, *ACS Nano* **2019**, *13*, 3353.
- [20] K. Y. Lee, S.-J. Park, D. G. Matthews, S. L. Kim, C. A. Marquez, J. F. Zimmerman, H. A. M. Ardoña, A. G. Kleber, G. V. Lauder, K. K. Parker, *Science* **2022**, *375*, 639.
- [21] Y. Alapan, O. Yasa, B. Yigit, I. C. Yasa, P. Erkoç, M. Sitti, *Annu. Rev. Control, Rob., Auton. Syst.* **2019**, *2*, 205.
- [22] M. A. Titus, H. V. Goodson, *J. Cell Biol.* **2017**, *216*, 1509.
- [23] W. F. Loomis, D. Fuller, E. Gutierrez, A. Groisman, W.-J. Rappel, *PLoS One* **2012**, *7*, e42033.
- [24] N. Kamprad, H. Witt, M. Schröder, C. T. Kreis, O. Bäumchen, A. Janshoff, M. Tarantola, *Nanoscale* **2018**, *10*, 22504.
- [25] Y. Artemenko, T. J. Lampert, P. N. Devreotes, *Cell. Mol. Life Sci.* **2014**, *71*, 3711.
- [26] P. Friedl, S. Borgmann, E.-B. Bröcker, *J. Leukocyte Biol.* **2001**, *70*, 491.
- [27] H. Ishikawa-Ankerhold, J. Kroll, D. van den Heuvel, J. Renkawitz, A. Müller-Taubenberger, *Cells* **2022**, *11*, 1776.
- [28] J. Shao, M. Xuan, H. Zhang, X. Lin, Z. Wu, Q. He, *Angew. Chem., Int. Ed.* **2017**, *56*, 12935.
- [29] X. Xu, M. Pan, T. Jin, *Front. Cell Dev. Biol.* **2021**, *9*, 724940.
- [30] K. F. Swaney, C.-H. Huang, P. N. Devreotes, *Annu. Rev. Biophys.* **2010**, *39*, 265.
- [31] B. Cichocki, R. Jones, *Phys. A: Stat. Mech. Appl.* **1998**, *258*, 273.
- [32] M. Tanaka, K. Fujimoto, S. Yumura, *Front. Cell Dev. Biol.* **2020**, *8*, 238.
- [33] M. Hörning, T. Shibata, *Biophys. J.* **2019**, *116*, 372.
- [34] H. Roth, M. Samereier, G. Trommler, A. A. Noegel, M. Schleicher, A. Müller-Taubenberger, *Biochem. Biophys. Res. Commun.* **2015**, *467*, 730.
- [35] O. Nagel, C. Guven, M. Theves, M. Driscoll, W. Losert, C. Beta, *PLoS One* **2014**, *9*, e113382.
- [36] J. Dalous, E. Burghardt, A. Müller-Taubenberger, F. Bruckert, G. Gerisch, T. Bretschneider, *Biophys. J.* **2008**, *94*, 1063.
- [37] R. Cornish, *Proc. R. Soc. Lond. Ser. A* **1928**, *120*, 691.
- [38] D. Holmes, J. Vermeulen, *Chem. Eng. Sci.* **1968**, *23*, 717.
- [39] E. Décavé, D. Garrivier, Y. Bréchet, B. Fourcade, F. Bruckert, *Biophys. J.* **2002**, *82*, 2383.
- [40] E. Décavé, D. Rieu, J. Dalous, S. Fache, Y. Bréchet, B. Fourcade, M. Satre, F. Bruckert, *J. Cell Sci.* **2003**, *116*, 4331.
- [41] R. B. Jones, *J. Chem. Phys.* **2004**, *121*, 483.
- [42] B. Cichocki, R. B. Jones, R. Kutteh, E. Wajnryb, *J. Chem. Phys.* **2000**, *112*, 2548.
- [43] J. D. Dunn, C. Bosmani, C. Barisch, L. Raykov, L. H. Lefrançois, E. Cardenal-Muñoz, A. T. López-Jiménez, T. Soldati, *Front. Immunol.* **2018**, *8*, 1906.
- [44] M. Clarke, U. Engel, J. Giorgione, A. Müller-Taubenberger, J. Prassler, D. Veltman, G. Gerisch, *BMC Biol.* **2010**, *8*, 154.
- [45] M. Prass, K. Jacobson, A. Mogilner, M. Radmacher, *J. Cell Biol.* **2006**, *174*, 767.
- [46] J. Zimmermann, C. Brunner, M. Enculescu, M. Goegler, A. Ehrlicher, J. Käs, M. Falcke, *Biophys. J.* **2012**, *102*, 287.
- [47] K. Yoshida, T. Soldati, *J. Cell Sci.* **2006**, *119*, 3833.
- [48] L. Pieuchot, J. Marteau, A. Guignandon, T. D. Santos, I. Brigaud, P.-F. Chauvy, T. Cloatre, A. Ponche, T. Petithory, P. Rougerie, M. Vassaux, J.-L. Milan, N. T. Wakhloo, A. Spangenberg, M. Bigerelle, K. Anselme, *Nat. Commun.* **2018**, *9*, 3995.
- [49] N. Srivastava, D. Traynor, M. Piel, A. J. Kabla, R. R. Kay, *Proc. Natl. Acad. Sci. USA* **2020**, *117*, 2506.
- [50] S. Krishnamoorthy, Z. Zhang, C. Xu, *Bio-Des. Manuf.* **2020**, *3*, 60.
- [51] Z. Sadjadi, D. Vesperini, A. M. Laurent, L. Barnefske, E. Terriac, F. Lautenschläger, H. Rieger, *Biophys. J.* **2022**, *121*, 4615.
- [52] C. A. Copos, S. Walcott, J. C. del Álamo, E. Bastounis, A. Mogilner, R. D. Guy, *Biophys. J.* **2017**, *112*, 2672.
- [53] H. Delanoë-Ayari, J. P. Rieu, M. Sano, *Phys. Rev. Lett.* **2010**, *105*, 248103.
- [54] E. Bastounis, R. Meili, B. Álvarez-González, J. Francois, J. C. del Álamo, R. A. Firtel, J. C. Lasheras, *J. Cell Biol.* **2014**, *204*, 1045.
- [55] B. Álvarez-González, R. Meili, E. Bastounis, R. A. Firtel, J. C. Lasheras, J. C. del Álamo, *Biophys. J.* **2015**, *108*, 821.
- [56] D. Arcizet, S. Capito, M. Gorelashvili, C. Leonhardt, M. Vollmer, S. Youssef, S. Rappl, D. Heinrich, *Soft Matter* **2012**, *8*, 1473.
- [57] M. Benoit, H. E. Gaub, *Cells Tissues Organs* **2002**, *172*, 174.
- [58] N. Otsu, *IEEE Trans. Syst., Man, Cybern.* **1979**, *9*, 62.
- [59] J. C. Crocker, D. G. Grier, *J. Colloid Interface Sci.* **1996**, *179*, 298.
- [60] C. Xu, J. Prince, *IEEE Trans. Image Process.* **1998**, *7*, 359.
- [61] M. K. Driscoll, C. McCann, R. Kopace, T. Homan, J. T. Fourkas, C. Parent, W. Losert, *PLoS Comput. Biol.* **2012**, *8*, e1002392.
- [62] V. Lepro, *Dissertation*, Universität Potsdam, Potsdam **2021**.